Application of Positron Emission Particle Tracking (PEPT) to measure the bubble-particle interaction in a turbulent and dense flow

Sommer, A.-E.; Ortmann, K.; van Heerden, M.; Richter, T.; Leadbeater, T.; Cole, K.; Heitkam, S.; Brito-Parada, P. R.; Eckert, K.;

Originally published:

September 2020

Minerals Engineering 156(2020), 106410

DOI: https://doi.org/10.1016/j.mineng.2020.106410

Perma-Link to Publication Repository of HZDR:

https://www.hzdr.de/publications/Publ-30763

Application of Positron Emission Particle Tracking (PEPT) to measure the bubble-particle interaction in a turbulent and dense flow

A.-E. Sommer[a,*], K. Ortmann[a], M. Van Heerden[b], T. Richter[a], T. Leadbeater[b], K. Cole[b], S. Heitkam[a,c], P.R. Brito-Parada[d], K. Eckert[a,c]

[a] *Helmholtz-Zentrum Dresden-Rossendorf, Institute of Fluid Dynamics, Bautzner Landstrasse 400, 01328 Dresden, Germany*
[b] *Department of Physics, University of Cape Town Rondebosch, 7700, South Africa*
[c] *Technical University Dresden, Institute of Process Engineering and Environmental Technology, 01062 Dresden, Germany*
[d] *Department of Earth Science and Engineering, Imperial College London, South Kensington Campus, London SW7 2AZ, United Kingdom*

Abstract

In a flotation cell, turbulence influences the motion of solid particles relative to the bubble surface, and, thus, affects the recovery rate. But, the impact of turbulence on the probability of a bubble-particle aggregation is still difficult to measure, especially in a dense flow. Therefore, the focus of this work was to apply Positron Emission Particle Tracking (PEPT) as a method to investigate the effect of turbulence on the particle movement and bubble-particle interaction in an opaque flow. Single air bubbles ($d_b = 2.5\,\mathrm{mm}$) were generated on a needle in a water flow channel. Upstream, a grid produced an isotropic turbulent flow with 5 % to 15 % turbulence intensity and a Kolmogorov microscale of 20 µm. Depending on the distance to the grid, the flow near the captive bubble ($Re_b \approx 450$) was characterized by eddies of different length scales and magnitude with tomographic Particle Image Velocimetry (PIV). The solid suspension contained up to 0.3 % polymethylmethacrylate (PMMA) particles ($d_p = 200\,\mu\mathrm{m}$–$400\,\mu\mathrm{m}$) and up to six radiolabelled particles ($d_p = 300\,\mu\mathrm{m}$–$400\,\mu\mathrm{m}$) coated with PMMA. The trajectories of the labelled particles were used to determine the average particle distribution in the turbulent field and describe the bubble-particle interactions. These results provide valuable information on the applicability of PEPT in turbulent and dense flow fields as well as on particle trajectories close to bubbles, enhancing our understanding of key flotation phenomena.

Keywords: Positron Emission Particle Tracking (PEPT), tomographic tomographic Particle Image Velocimetry (PIV), bubble-particle interaction, grid turbulence, dense flow, flotation

1. Introduction

Flotation is one of the most important processes for the separation of valuable minerals from gangue material. For an efficient process, a high collision rate must occur between particles and bubbles where turbulence is a significant factor (Fallenius, 1987; Schubert, 1999; Nguyen and Schulze, 2003; Evans et al., 2008). Nguyen et al. (2016) divided the effect of turbulence depending on the eddy size into macro- and microturbulence. Although, the large scale eddies of the macroturbulence break-up and their energy is transferred into small scale eddies of the microturbulence as described with the energy cascade. At the smallest scale, the Kolmogorov scale, the eddies dissipate. The macroturbulence controls the large-scale material transport in the size range of the flotation cell, whereas the microturbulence affects the motion of bubbles and particles. Consequently, turbulence influences the frequency of bubble-particle collision and, thus, the recovery in a flotation cell. A deeper understanding of the influence of turbulence on bubble-particle interactions is therefore important to improve the efficiency of the flotation process.

*Corresponding author
Email address: a.sommer@hzdr.de (A.-E. Sommer)

However, there is a limited number of studies which focus on the influence of the conditions in a flotation on the individual bubble-particle interaction, namely a dense and turbulent flow. So far, studies investigated either the individual bubble-particle interaction in a quiescent flow without turbulence (Nguyen and Kmeť, 1992; Nguyen and Schulze, 2003; Basařová et al., 2010), or the influence of turbulence on multiphase flows in a flotation cell (Hassanzadeh et al., 2018). One reason for the lack is the opaqueness of the concentrated particle-bubble-dispersion (Meng et al., 2016) which prevents the usage of optical measurement techniques. Therefore, Brady et al. (2006) used low gas and solid fractions to investigated the influence of turbulence on the velocity of particles and bubbles using a time-resolved Particle Image Velocimetry (PIV) and Particle Tracking Velocimetry (PTV) system. For a reproducible turbulent flow field, a water channel was used, where isotropic turbulence was generated by a grid. However, these measurements are less comparable to the multiphase flow with a high solid fraction in a flotation cell because the generation and dissipation of turbulence due to particles are neglected (Hetsroni, 1989).

In spite of an optical particle tracking method, Positron Emission Particle Tracking (PEPT) is often used as a measurement technique for opaque flows (Parker et al., 1993; Leadbeater et al., 2012). First, a tracer particle is radiolabelled with a positron emitting radionuclide, which undergoes a beta-plus decay. This, in turn, emits two photons in anti-parallel directions after annihilation with local electrons. If two detectors in an array simultaneously detect these gamma rays in coincidences, a line of response (LOR) can be defined between the two detection points. A sample of consecutive LORs (typically 150 to 1000 events) are used to triangulate the instantaneous position of the tracer particle in three dimensions. Several studies have successfully applied PEPT to measure the particle velocity field within the pulp and froth phase of a flotation cell (Boucher et al., 2017; Cole et al., 2012; Waters et al., 2008, 2009). So far, this method has only been used to determine the position of tracer particles and not bubbles. Thus, a simultaneous measurement with a high-speed camera (Cole et al., 2010b) or a prescribed bubble position is necessary to describe the interaction between bubbles and particles.

The goal of the present study was to establish a method to measure the effect of turbulence on the individual bubble-particle interaction in a dense flow. Therefore, the applicability of PEPT was investigated as the only particle tracking technique for an opaque flow. The turbulence was generated using a grid upstream of a bubble in a water channel. This setup produced similar small-scale turbulent structures as in a flotation cell but in a defined and reproducible way (Comte-Bellot and Corrsin, 1971). For the application of PEPT, the bubble was fixed to a needle, as described in the investigations of Nguyen and Kmeť (1992) and Basařová et al. (2010).

The study was separated into two parts based on the applied measurement technique - tomographic PIV and PEPT. Firstly, the turbulent behaviour of the flow, including the time-averaged velocity profile, the turbulence intensities and the energy spectrum in the water channel, was characterized by tomographic PIV. The analysis identified the range of turbulent length scales and the quality of the isotropic turbulence produced by the grid. Secondly, a solid polymethylmethacrylate (PMMA) suspension including radiolabelled tracers was added to the flow of the water channel to measure with PEPT the influence of turbulence on the bubble-particle interaction. Hereby, the analysis focused not only on the particle distribution within the cross-sectional area of the water channel but also on the deviation of particle trajectories closely by the stagnant bubble. Finally, the divergent particle trajectories were classified according to their potential interaction with the bubble based on their residence time.

2. Experimental setup

2.1. Turbulent flow in a water channel

The experiments were performed in a water channel where a large range of turbulent length-scales was generated by a grid upstream of a bubble, as seen in Fig. 1(a). The setup was adapted from the investigations from Haase et al. (2017) and Tokuhiro et al. (1998) who produced similarly a downward flow in a water channel. The flow recirculated from the upper tank through the water channel into the lower tank, where the suspension was pumped upwards again by a peristaltic pump (Watson Marlow, 730SN/RE). In order to ensure a uniform suspension of the particles, a mechanical stirrer was installed in the upper tank. Excess

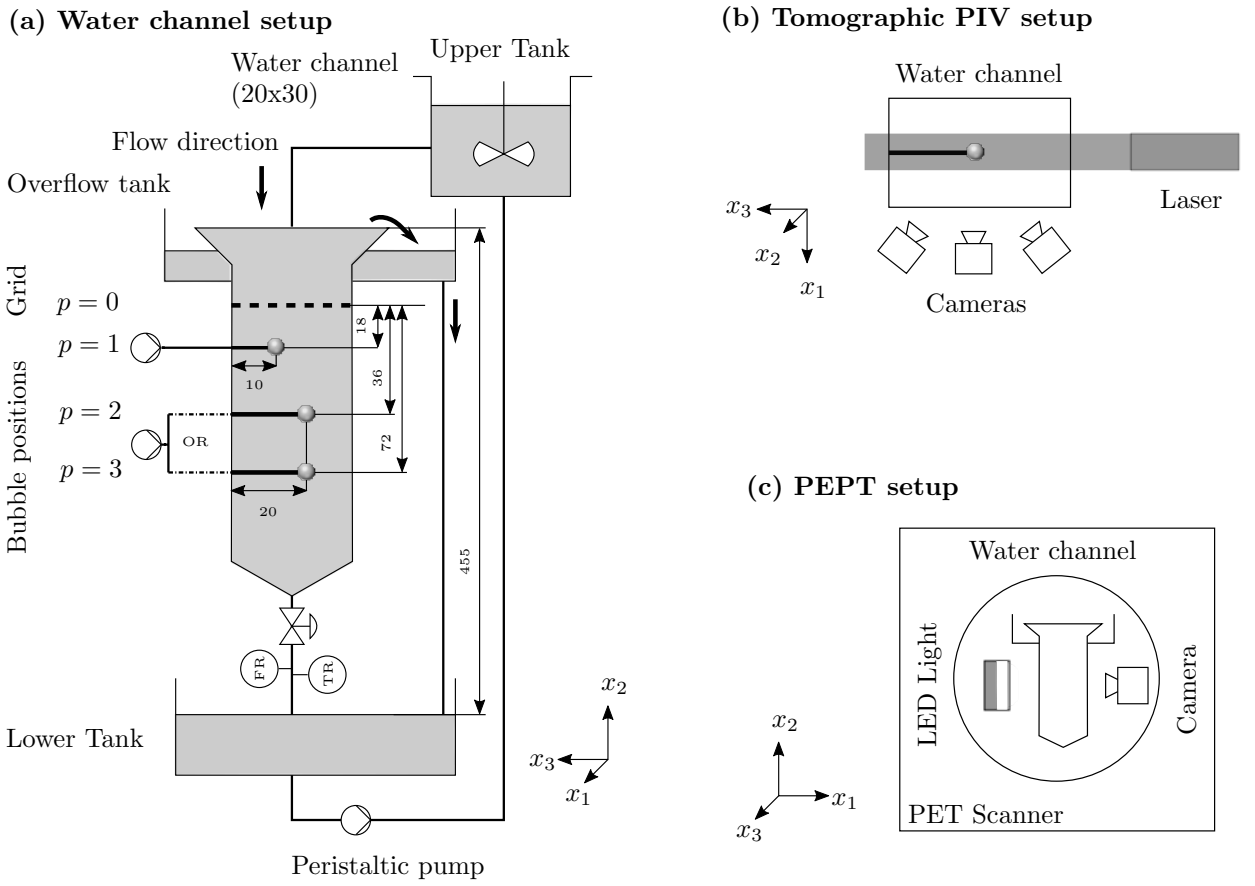

Figure 1: Experimental setup: A grid generated turbulent inflow condition on stagnant bubbles inside the water channel (a). The downwards flow was set by an electrical valve and controlled by a volumetric flowmeter (FR) and an integrated temperature sensor (TR). The flow recirculated by pumping the suspension upwards into the upper tank with a peristaltic pump. Units are displayed in mm.
Arrangement of the water channel in the tomographic PIV (b) and the PEPT setup (c). All illustrated configurations and measurement systems are matched to coordinate system of the Positron Emission Tomography (PET) scanner.

suspension, which could not fit into the water channel, flowed over the overflow tank directly into the lower tank to remain in the system. Consequently, the water height was kept automatically constant, and thus, the flow rate depended only on the valve position. During the experiments, the valve was completely open resulting in a flow rate of $Q = 6.1\,\mathrm{l/min}$. This rate was checked with a volumetric flowmeter and an integrated temperature sensor (Sika, VTI 15) during all measurements.

Besides a wide range of turbulent length-scales, a grid has the advantage of producing isotropic turbulence, as shown by Kurian and Fransson (2009). Likewise, a grid with cylindrical rods, $d_r = 1\,\mathrm{mm}$, and a mesh width, $M = 3.2\,\mathrm{mm}$, was used to achieve a Kolmogorov length scale, η, of $20\,\mu\mathrm{m}$. The Kolmogorov length scale was estimated as

$$\eta = d_r(Re_d)^{-3/4}, \tag{1}$$

with $Re_d = 180$ as the Reynolds number based on the rod diameter. The range of turbulent length scales and their intensity depended on the distance to the grid, according to the energy cascade. With increasing distance to the grid, larger vortices broke down to smaller ones and the smallest eddies disappeared. Consequently, bubbles were placed at three distances to the grid ($p = 1{-}3$ in Fig. 1(a)) for different turbulent inflow conditions. Special care was taken to fix the bubble position in x_1- and x_3- direction, directly downstream from a loop of the grid, in order to generate symmetrical conditions. Each bubble ($d_b = (2.5 \pm 0.3)\,\mathrm{mm}$) was produced individually with a needle ($d_a = 0.9\,\mathrm{mm}$) and a syringe pump to control their size independently (New Era Pump Systems, Inc., NE-1000 or Harvard Apparatus, Pump 33). To hinder the detachment of a bubble, the needles were hydrophobized with tetradecyltrimethylammonium bromide (TTAB, purchased by Sigma-Aldrich). Accordingly, the needles were placed into the TTAB solution ($c = 4.14\,\mathrm{g\,l^{-1}}$) overnight. Before the installation in the water channel, each needle was rinsed carefully with deionized water to remove excess surfactant.

The main challenge of this setup was that only the interaction of individual radiolabeled particles with individual bubbles was observable with this technique. Therefore, the potential for a collision between bubble and particle was increased by employing two bubbles simultaneously at two of the three possible vertical positions. The horizontal separation between both bubbles was 10 mm to minimize the effect of the upper bubble on the lower one. This doubled the probability of a bubble-particle collision, P_{coll}, from 0.8 % to 1.6 % per tracer passage. The values are quantified by the observation from Nguyen and Schulze (2003), where only particles within the grazing trajectory of the bubble led to a collision,

$$P_{coll} = \frac{n_b \cdot A_b}{A_{wc}} \cdot 100, \tag{2}$$

with the number of bubbles n_b, the cross-sectional area of the bubble, $A_b = \pi(d_b/2)^2$, and the cross-sectional area of the water channel, $A_{wc} = 600\,\mathrm{mm}^2$.

2.2. Solid suspension and radioactive tracer particles

The solids suspension within the channel consisted of $0.01\,\mathrm{mol\,l^{-1}}$ KCl and fluorescent PMMA spheres ($d_p = 200\,\mu$m-$400\,\mu$m; Re_p = 40-80, microParticles GmbH). These model particles were selected because of their defined size and shape, their hydrophobic wetting behaviour, and their applicability for other particle tracking methods as 4D PTV (Sommer et al., 2018) due to their fluorescent colour. The latter property was important for a subsequent comparison study between PEPT and other optical particle tracking techniques, which is not part of this study. Optical particle methods are limited to a dilute flow, while with PEPT, also particles in a dense flow are trackable. Consequently, only PEPT enables the study of the interaction between the particles in a dense flow. With regards to Sommerfeld (2017), the border between both systems is at a volume fraction of approximately $\phi = 0.05\,\%$. Therefore, two different volume fractions were used during these measurements. First, a dilute solid suspension with $\phi = 0.01\,\%$ and, second, a dense solid suspension with $\phi = 0.22\,\%$ was applied.

For the detection of individual particles with PEPT, tracer particles were designed to represent the bulk PMMA particles. These tracers had to fulfil two criteria. On the one hand, they had to be radioactive to be traceable within the Positron Emission Tomography (PET) scanner. On the other hand, the physical properties of the PEPT tracer had to be similar to the PMMA spheres in the suspension. To meet all these

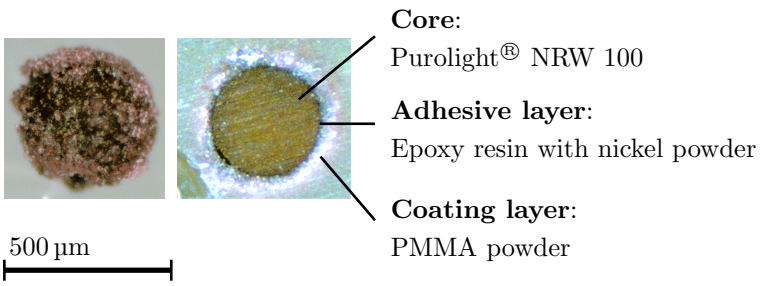

Figure 2: PEPT tracer (left) and micrograph of the same particle cutted, grinded and polished along its diameter (right). The latter one was used to distinguish the three parts, namely, the core, the adhesive layer and the coating layer.

criteria, the coating technique of Cole et al. (2014), which used a silica coating and cyanoacrylate as an adhesive, was adapted for PMMA. Accordingly, the tracer particle consisted of three parts, including a core in form of an ion exchange resin, an adhesive layer containing epoxy resin, and a PMMA coating layer, as seen in Fig. 2.

The core was composed of Purolight® NRW 100, an adapted spherical ion exchange resin for labelling with ^{68}Ga. For the labelling, the techniques developed at PEPT Cape Town (Cole et al., 2012), were used and achieved a tracer activity of $I = (850 \pm 200)\,\mu$Ci at the beginning of each measurement. The adhesive layer was modified to prevent the dissolution of PMMA particles within the epoxy resin and provide additional physical strength of the coating to withstand the high stresses within the peristaltic pump. Therefore, a mixture of an epoxy resin and a nickel powder, each with a volume fraction of 50 %, was applied. Finally, the tracer particle was coated with fluorescent PMMA powder (d_p = 1 µm–20 µm) as an outer layer. A heat-treatment was applied during tracer fabrication so that the coating was completely cured before the tracers were added to the channel. The heat-treatment included three intervals of 15 s heating at 160 °C to 180 °C and 15 s cooling at room temperature.

During the measurements, up to six radioactive particles were added to the water channel. The rather high number of radioactive tracer was chosen to increase the rate of bubble-particle interactions. The high residence time of the radioactive tracers within the whole system, $\Delta t_{tot} \approx 1$ min, made it unlikely that multiply radioactive tracers were in the region of interest (ROI), $\Delta t_{ROI} \approx 1$ s.

To conclude from the individual PEPT particle to the overall PMMA suspension, their physical properties had to be similar. Therefore, Tab. 1 summarizes the physical properties of both particle types, in form of the surface material, the diameter, d_p, the density, ρ_p, and the relaxation time, τ_p. The latter one represents the required time for a particle to adjust its velocity to sudden changes in the surrounding flow field (Nguyen and Schulze, 2003) and is defined as

$$\tau_p = \frac{\rho_p d_p^2}{18\mu}, \tag{3}$$

with μ the dynamic viscosity. Furthermore, the ratio of the relaxation time to the characteristic time scale of the flow, τ_l, is called Stokes number,

$$St = \frac{\tau_p}{\tau_l} \tag{4}$$

and evaluates how closely a particle follows the fluid streamlines. In the case of $St < 1$, particles follow the fluid streamlines closely, whereas in the case $St > 1$, particles detach from a flow especially due to abrupt velocity changes (e.g. turbulences) (Nguyen and Schulze, 2003). Given these points, the PMMA tracers have smaller inertia and drag than the PEPT tracers. Regardless of this, the PEPT tracers are comparable and follow similarly the turbulent flow in the water channel.

Property	Solids suspension	PEPT tracer
Surface material	fluorescent PMMA	fluorescent PMMA powder ($d_p = 1\,\mu$m–$20\,\mu$m)
d_p in μm	200–400	300–400
ρ_p in g cm^{-3}	1.18	1.5 ± 0.2
τ_p in ms	2.7–10.7	7.5–21.3

Table 1: Properties of PEPT tracers and PMMA particles. The particle types are compared in terms of their surface material, diameter, d_p, density, ρ_p, and relaxation time, τ_p. The latter one represents the required time for a particle to adjust its velocity to sudden changes in the surrounding flow field (Eq. 3).

3. Tomographic PIV

3.1. Single-phase liquid flow field

The single-phase liquid flow field in the water channel was measured with tomographic PIV. The basic idea of PIV is that sufficiently small and neutrally buoyant particles follow the streamlines of the fluid flow with negligible deviation. Thus, the fluid velocity is assumed to be equal to the particle velocity. In the case of tomographic PIV, the particles within a defined volume are illuminated by a laser and the scattered light is captured with three cameras from different angles. The three viewing angles lead to a reconstruction of the particle field as a 3D distribution of light in the form of volume elements, called voxels. For each voxel, a 3D cross-correlation method calculates the 3D-3C velocity field, resolving the instantaneous velocity field, $\mathbf{u} = (u_1, u_2, u_3)^T$, in all three directions, $\mathbf{X} = (x_1, x_2, x_3)^T$. A detailed review of this technique is given by Scarano (2012).

During the experiment, images were taken with three CMOS cameras (Phantom VEO 410 L, spatial resolution 0.04 mm/px) in combination with a Nd:YAG laser (Photonic Industries, wavelength $\lambda = 532$ nm). The illuminated volume, with a thickness of 10 mm, was placed perpendicular to the channel and was aligned to the needle position. Fluorescent PMMA particles (microParticles GmbH) in the size range from 20 µm to 50 µm were used as tracer particles. The measurements were time-resolved with a recording rate of $F = 2000$ fps over 1.5 s. The data were evaluated with the commercial software DaVis 10.1 (LaVision), using an interrogation window size of 32 px × 32 px after an iterative multigrid evaluation with interrogation window refinement.

The tomographic PIV measurement provided results in the form of a time-resolved instantaneous velocity field for all three dimensions. The coordinate system of the setup, $\mathbf{X} = (x_1, x_2, x_3)$, was defined by the positioning of the water channel within the PET scanner (Fig. 1(b)). The x_2-direction pointed against the main flow direction, the x_1- and x_3-direction were orthogonal to that, providing x_3 as the horizontal direction of the needle. Therefore, the highest velocities were in u_2. To characterize the liquid flow field within the water channel, the instantaneous velocity field, $\mathbf{u}$, was decomposed into its mean velocity, $\overline{\mathbf{u}}$, and its fluctuations, $\mathbf{u}'$, as $\mathbf{u} = \overline{\mathbf{u}} + \mathbf{u}'$. For this, the instantaneous velocity field was time-averaged over $N = 3000$ consecutive time steps. The fluctuations were used to compute the degree of turbulence, Tu_{ij} with $i, j \in 1, 2, 3$, within the water channel as

$$Tu_{ij} = \frac{\sqrt{R_{ij}}}{|\overline{\mathbf{u}}|}, \tag{5}$$

with the Reynolds stress tensor component, $R_{ij} = u_i' \cdot u_j'$. Furthermore, the range of turbulent length-scales in the liquid flow was determined by the power spectrum, $\Psi_i(f)$. The power spectrum is the discrete-time Fourier transform of the fluctuation component, $u_i'(x_1, x_2, x_3, t)$, at a given point, $\mathbf{X} = (x_1, x_2, x_3)^T$, leading to the transformation of the data from the time, t, into the frequency domain, f. Each spectrum was calculated based on 500 time steps.

3.2. Uncertainty analysis

During the measurements, random uncertainties occurred e.g. due to the particle image size, particle image density, turbulent fluctuations, and interrogation window size. Therefore, the uncertainties of the average velocity, $U_{\overline{u_i}}$, and degree of turbulence, $U_{Tu_{ij}}$, were quantified within a confidence interval of 95.4 % as

$$U_{\overline{u_i}} = 2.0 \cdot \sigma_i \sqrt{\frac{1}{N}}, \tag{6}$$

with the standard deviation, $\sigma_i = \sqrt{\frac{1}{N-1} \sum_{i=1}^{N} (u_i - \overline{u_i})^2}$. The uncertainty of the degree of turbulence, $U_{Tu_{ij}}$, was calculated based on the propagation of uncertainty, incorporating the uncertainty of Reynolds stress,

$$U_{R_{ij}} = \sigma_i \sigma_j \sqrt{\frac{1 + \rho_{ij}^2}{N-1}}, \tag{7}$$

with the cross-correlation coefficient, ρ_{ij}. This yields

$$U_{Tu_{ij}} = \left| \frac{\partial Tu_{ij}}{\partial R_{ij}} \right| \cdot U_{|\overline{\mathbf{u}}|} + \left| \frac{\partial Tu_{ij}}{\partial |\overline{\mathbf{u}}|} \right| \cdot U_{R_{ij}} \tag{8}$$

$$= \left| \frac{1}{2\sqrt{R_{ij}}} |\overline{\mathbf{u}}| \right| \cdot U_{|\overline{\mathbf{u}}|} + \left| \frac{-\sqrt{R_{ij}}}{|\overline{\mathbf{u}}|^2} \right|. \tag{9}$$

This method for analyzing the uncertainty of PIV measurements has been described by Sciacchitano and Wieneke (2016), further details can be found there.

For the calculation of the power spectrum, the resolution of the turbulent length scales are limited by the interrogation window size, $IW = 32$ px, which is comparable to a low-pass filter. Depending on the interrogation window size, IW, Foucaut et al. (2004) gives a maximum resolvable cut-off frequency, f_c, as

$$f_c = \frac{2.8}{IW} \cdot |\overline{\mathbf{u}}| = 396\,\mathrm{Hz}. \tag{10}$$

However, the cut-off frequency represents only the upper limit of resolvable frequency (Atkinson et al., 2010). Due to noise within the tomographic PIV measurement, the maximum measured frequency can be smaller.

4. Positron Emission Particle Tracking

4.1. Detection of the bubble position with high-speed imaging

The experiments of the bubble-particle interactions in a turbulent flow used a combination of PEPT and high-speed (HS) imaging. PEPT tracked the particle trajectory throughout the experimental setup and the HS camera recorded the position, $x_{2,b,i}$ and $x_{3,b,i}$, and size of both bubbles, $d_{b,i}$. In that way, the HS camera checked continuously the bubble properties to account for small changes. Although, the stagnant bubble approach defined the bubble position within the water channel, and thus, in the PET scanner. But, small changes in the position of the water channel or needle would be excluded by only a daily calibration.

For the experiments, the water channel was centered in the PET camera, ECAT HR++ (Model: CTI/Siemens), at iThemba LABS, South Africa (Buffler et al., 2010) (Fig. 1(c)). The HS camera (Jai GO-5100M-USB) was located parallel to the water channel wall to capture both bubbles in the x_2-x_3 plane. During the image analysis, a Hough transformation (Davies, 2004; Yuen et al., 1990) was applied to detect the stagnant bubble as a circle and obtain its properties. Both systems were calibrated with a PEPT tracer glued to a needle tip and placed within the water channel at all three positions, p. Simultaneously, the known particle location was recorded by both systems, PEPT and HS camera, leading to an alignment of both coordinate systems with an uncertainty lower than 2 mm.

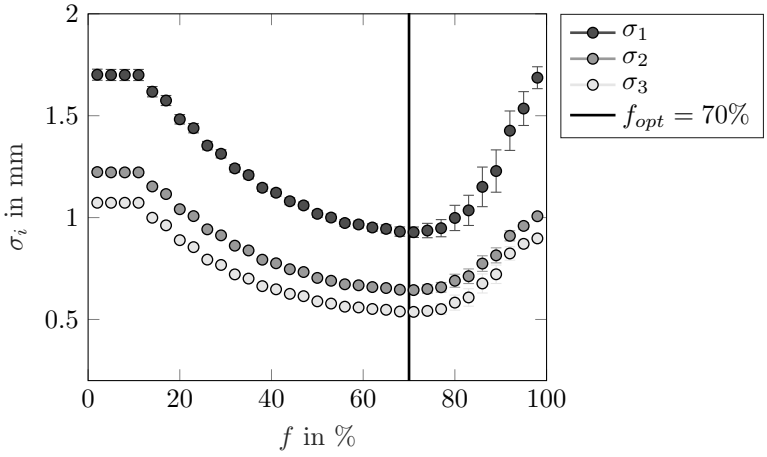

Figure 3: Uncertainty of the triangulated position of a PEPT tracer. The standard deviation, σ_i, of a stationary source depending on the proportion of corrupted LORs, f, evaluated in all three directions ($i = 1 - 3$). The stationary source was a PEPT tracer glued to a needle tip and was placed one after another at each bubble position in the water channel (Fig. 1). For the triangulation, the specific number of LORs $N = 50$ was used.

4.2. Particle triangulation

The inserted radiolabeled tracer was triangulated using the algorithm of Parker et al. (1993), adapted to the PEPT Cape Town system and described by Buffler et al. (2010). The algorithm required the specific number of LORs, N, and the proportion of corrupted events, f_{opt} which are specific for the individual setup and tracer activity. Both values were optimized regarding the temporal and spatial resolution of the PEPT tracer location. In respect of the temporal resolution, the goal was to achieve the maximum temporal resolution, $\Delta t = 1\,\text{ms}$, based on the location rate of the PET camera ($F = 1000\,\text{Hz}$), for each particle trajectory. However, the exponential decay of the tracer radionuclide decreased the rate of an emitting positron, and thus, the temporal resolution. Therefore, the initial number of LORs per slice, $N = 1000$, was reduced continuously with decreasing tracer activity until $N = 50$ to calculate the particle location and time. Further, the sliding window technique from Sovechles et al. (2017) was applied to increase artificially the number of LORs, due to the usage of previously processed LORs. The overlap of adjacent LOR ranged between 0 % and 75 %. If the temporal resolution of the particle trajectory exceeded 3 ms, the data were discarded for further calculations.

Besides an optimal number, N, also the proportion of corrupted events of LORs, f, is needed to achieve a high spatial resolution. Consequently, the influence of f on the standard deviation in tracer location, σ_i, was measured with a stationary source under controlled conditions (Leadbeater et al., 2012). Fig. 3 illustrates the results for a PEPT tracer glued to a needle tip which was placed one after another at each bubble position in the water channel (Fig. 1). The number of LORs was kept constant at 50, leading to the global minimum at $f_{opt} = 70\,\%$.

Finally, the particle trajectory was smoothed and interpolated with the method from Cole et al. (2010a). Cole et al. (2010a) used a time weighting function with a cubic spline to remove noise. Likewise, the kernel width was adapted to 10 ms, which is slightly less than the average residence time of a particle flowing around a bubble ($\Delta t \approx d_b/|\overline{\mathbf{u}}| \approx 14\,\text{ms}$).

However, this triangulation method was developed for only one single PEPT tracer within the PET camera at a time. In order to take multiple particles into account, a ROI was set in the channel to avoid the interference of two or more particles on the triangulation of any single tracer location. The ROI was defined as a sphere with the bubble centre coordinates, $\mathbf{X_b} = (x_{1,b}, x_{2,b}, x_{3,b})^T$, and radius, r_{ROI}, which was evaluated separately for each bubble position, p. Therefore only instances of LORs crossing the ROI were used for the triangulation of a particle. If multiple particles were in the ROI, their trajectories were rejected for further data analysis. The ROI radius was defined as $r_{ROI} = 9d_b$, as a compromise between the

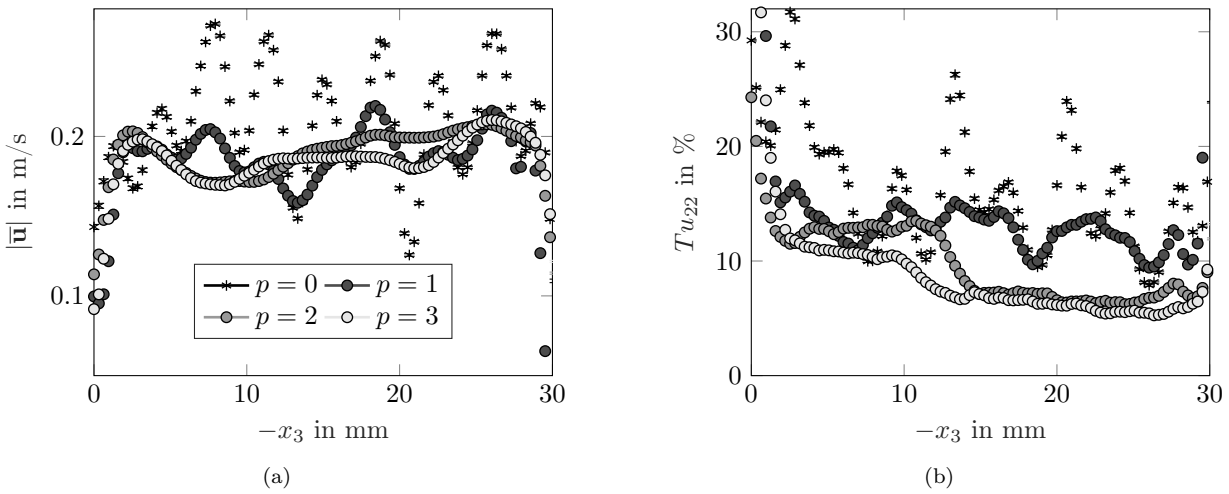

Figure 4: Turbulence characteristics measured with tomographic PIV in terms of (a) time-averaged velocity profile, $\overline{|\mathbf{u}|}$, and (b) degree of turbulence in x_2-direction, Tu_{22}. The properties are evaluated along the $-x_3$ direction where 0 mm and 30 mm define the channel walls. The position in x_1- and x_2-direction are defined by the location of the grid and the bubble, $p = 0 - 3$ (Fig. 1).

enhancement of the small evaluation volume to increase the probability of detecting multiple particles and minimizing particle tracking errors close to the ROI boundaries.

4.3. Uncertainty analysis

The uncertainty of the PEPT measurement method had three components - a random triangulation error, a random experimental setup error and a systematic calibration error. The triangulation uncertainty was caused by physical effects in the measurement system, including low angle photon scatter and detector spatial resolution. In Fig. 3 the uncertainty ranged between 0.5 mm and 1 mm, depending on the direction, for the applied f_{opt} value of 70 %.

The experimental setup uncertainty was caused e.g. due to a small variation of the concentration of the solid suspension, the properties of the tracer particle, the temperature or the flow. The uncertainty was quantified statistically by repeated measurement of the same experimental parameters, but a different set of tracer particles. The population of repetitions varied between four and nine times, depending on the experimental parameter.

The calibration error included the positioning of the water channel in the PET scanner based on six reference points and the location of the bubble. The latter one was only checked in the x_2-x_3-plane, and not in the x_1-x_2 and x_1-x_3-planes because of the $2D$ HS camera image. The resulting uncertainties in the x_2 and x_3 dimension were estimated of the order of 1 mm, whereas in the x_1 position the uncertainty was approximated as 2 mm because of the limited verification with the HS camera during the measurements.

5. Results and Discussion

5.1. Turbulence characteristics measured with tomographic PIV

In the current setup, a grid was used to produce isotropic turbulence. Passing the grid, turbulent kinetic energy (TKE) was added to the large length scales as integral length scales, Λ, corresponding to the grid size. By the break-up of vortices, the energy was transferred to smaller length scales until they dissipated at the Kolmogorov scale, η. This led to a large range of turbulent length scales (Kurian and Fransson, 2009). To quantify them in the inflow of each bubble, tomographic PIV was used. From particular interest was the time-averaged velocity magnitude, $|\overline{\mathbf{u}}| = \sqrt{\overline{u}_1^2 + \overline{u}_2^2 + \overline{u}_3^2}$ (Fig. 4(a)), the degree of turbulence in the x_2-direction, Tu_{22}, (Fig. 4(b)) and the power spectra, Ψ_i (Fig. 5).

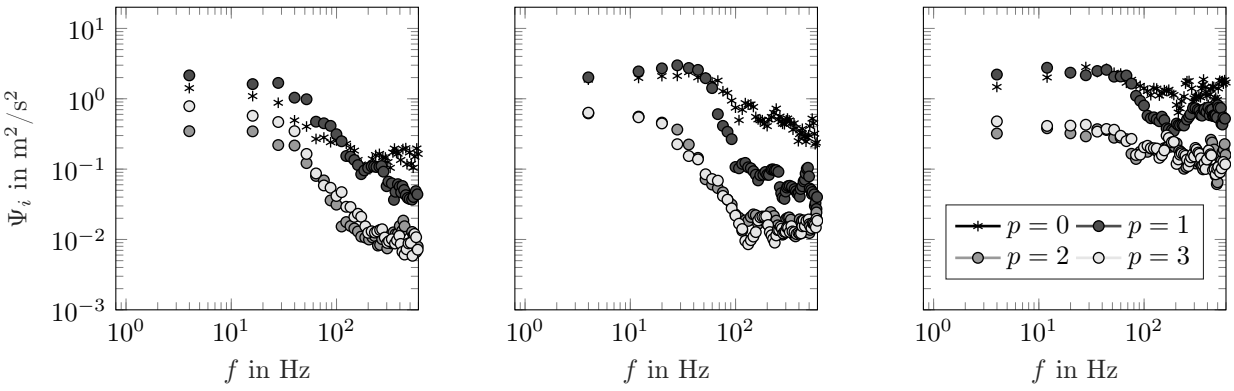

(a) $i = 1$ (b) $i = 2$ (c) $i = 3$

Figure 5: Power energy spectra measured with tomographic PIV in (a) x_1-direction, (b) x_2-direction and (c) x_3-direction. $p = 0 - 3$ defines the position in x_1 and x_2 direction which corresponds to the location of the grid and the bubble (see Fig. 1).

In Fig. 4, the time-averaged velocity magnitude, $|\overline{\mathbf{u}}|$, and the degree of turbulence in the x_2-direction, Tu_{22}, are plotted along the horizontal direction of the needle, x_3. The upper bubble position, $p = 1$, equaled $x_3 = -10\,\text{mm}$, and for the middle, $p = 2$, and lower one, $p = 3$, x_3 was $-20\,\text{mm}$ (Fig. 1). At these points, the time-averaged velocity magnitude was $0.18\,\text{m}\,\text{s}^{-1}$ (Fig. 4(a)). This velocity magnitude corresponded to the rising velocity of 2.5 mm bubbles in water (Clift et al., 2005), resulting in a Reynolds number of the bubble as $Re_b = 450$.

The degree of turbulence, Tu_{22}, decreased with increasing distance to the grid (Fig. 4(b)). The highest degree of turbulence was shortly after the position of the grid, $p = 0$, and varied between 10 % and 30 %. At this point, the turbulence was produced by the wake of the grid rods. At the upper bubble position, $p = 1$, one part of the TKE still remained in the large scales resulting into $Tu_{22} = 15\,\%$. These large length scales dissipated further downstream, at the middle, $p = 2$, and lower bubble position, $p = 3$, thus, Tu_{22} was 5 %. Due to the wake of the upper needle, a higher degree of turbulence was found in the left part of the channel corresponding to $x_3 > -10\,\text{mm}$.

The degree of turbulence quantified the turbulent intensity within the flow. But, the power spectrum represented the contribution of TKE by the eddy frequency, f, resulting in the quantification of isotropic turbulence and turbulent length scales (Fig. 5). Regarding the power spectrum, isotropic turbulence means that the TKE within the turbulent length scales are equivalent in all three dimensions. This case is reached in Ψ_1 (Fig. 5(a)) and Ψ_2 (Fig. 5(b)) at the middle, $p = 2$, and lower bubble position, $p = 3$. Although, Ψ_3 (Fig. 5(c)) was one order of magnitude higher at these positions. One reason could be the high uncertainty of u_3, resulting from the reconstruction process in the tomographic PIV algorithm. This uncertainty could add artificial turbulence to the spectrum. Leading to the conclusion, a status of nearly isotropic turbulence was achieved in the middle and lower bubble position.

The range of turbulent length-scales was bounded between the Kolmogorov length scale, η, and the integral length scale, Λ (Roach, 1987). Both were approximated with the Taylor hypothesis (Pope, 2000) from the temporal correlation of the power spectrum,

$$\eta = \frac{|\overline{\mathbf{u}}|}{f_\eta} = 0.6\,\text{mm} - 1.8\,\text{mm}, \tag{11}$$

$$\Lambda = \frac{|\overline{\mathbf{u}}|}{f_\Lambda} = 9\,\text{mm}, \tag{12}$$

with the corresponding frequency from the Kolmogorov scale, $f_\eta = 100\,\text{Hz} - 300\,\text{Hz}$, and from the integral length scale, $f_\Lambda = 4\,\text{Hz} - 40\,\text{Hz}$. The frequency from the Kolmogorov scale correlated to the smallest frequency before the stagnation of the power spectrum graph. Equally, the integral length scale corresponded

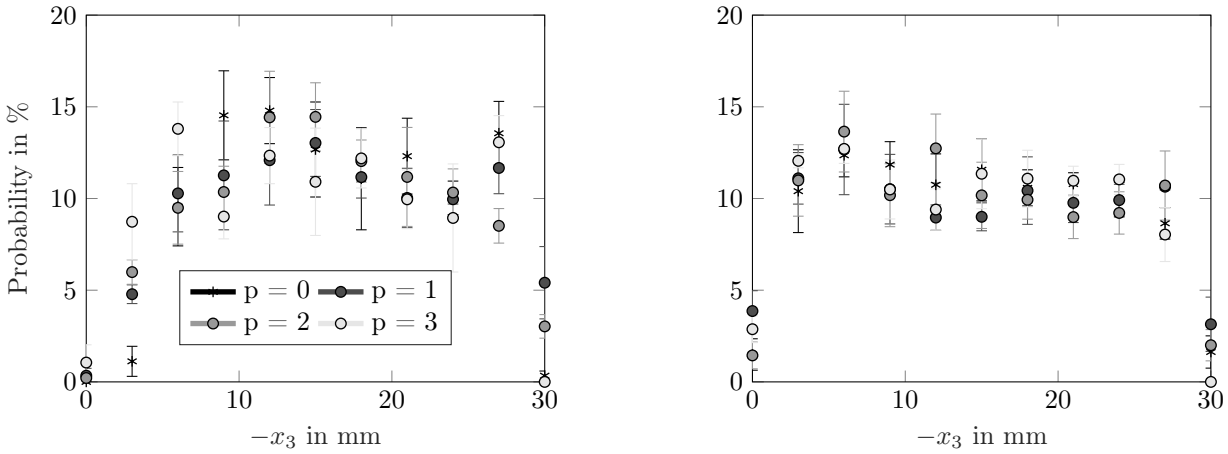

(a) $\phi = 0.01\,\%$ (b) $\phi = 0.22\,\%$

Figure 6: Probability of the tracer location along $-x_3$-direction measured with PEPT: A (a) dilute flow with a volume fraction of $\phi = 0.01\,\%$, and (b) A dense flow with $\phi = 0.22\,\%$. The trajectory of the tracer particles are binned over $x_1 = [-5, 5]$ mm. The x_2 direction corresponds to the location of the grid and the bubble (Fig. 1).

to the frequency of the maximum energy. However, the theoretical length scale range regarding the grid dimensions was

$$\eta = d_r(Re_d)^{-3/4} = 20\,\mu\text{m}, \tag{13}$$

$$\Lambda = |\overline{\mathbf{u}}|/\frac{Sr \cdot |\overline{\mathbf{u}}|}{d_r} = \frac{d_r}{Sr} = 4.8\,\text{mm}, \tag{14}$$

with the Reynolds number based on the diameter of the rod, $Re_d = 180$, and the Strouhal number for vortex shedding, $Sr = 0.21$. The difference between theoretical and experimental length scale ranges could be caused on the higher frequencies by the low-pass filter of the interrogation window size (Sec. 3.2) and on the lower limit by the oscillation of the peristaltic pump, $U = 100\,1/\text{min}$, which added artificial turbulence in the low frequency range. Therefore, the experimental setup could not measure and resolve all length scales down to the Kolmogorov scale.

Further is noted, that the measurement took place in a single-phase liquid flow. Therefore, the results are only partly transferable to a dense flow, as described in the following PEPT measurements. The solid suspension could cause a higher effective viscosity of the dispersion and affect the turbulent structures in the flow field (Hetsroni, 1989). Depending on the particle's Reynolds number Re_p, particles reduce ($Re_p < 400$) or increase ($Re_p > 400$) the turbulence level. Therefore, the turbulence level in this study should be reduced by adding the PMMA suspension ($Re_p = 40 - 80$).

5.2. Effect of turbulence on the particle distribution measured with PEPT

With PEPT, the effect of the turbulent length scales on the particle movement was investigated. The distribution in Fig. 6 describes the occupancy of tracer particles in the channel cross-section. As noted before, the tracer particles were designed to represent the bulk PMMA particles, thus, their probability indicates the distribution and concentration of PMMA particles. The distribution was measured around each bubble positions, p, as defined in Fig. 1, specifically, $x_1 = [-5, 5]$ mm and $x_3 = [-30, 0]$ mm. As Fig. 6 illustrates, the particles were equally distributed along x_3 for a low as well as for a high volume fraction. Any differences in vertical positions were of the order less than uncertainty. Close to the vertical walls, $x_3 = 0\,\text{mm}$ and $x_3 = -30\,\text{mm}$, a lower amount of particle passes is visible because of the low velocity in the boundary layer.

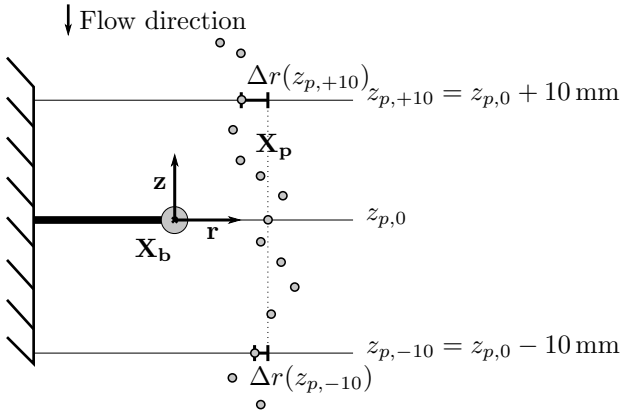

Figure 7: Illustration of the radial deviation, $\Delta r(z_p)$ of a tracer particle trajectory, $\mathbf{X_{p,c}} = (r_p, \theta_p, z_p)^T$, around a bubble, $\mathbf{X_b}$. Hereby, the radial deviation is defined as the distance between the reference point, $z_{p,0}$, and the comparison point, $z_{p,+10}$ or $z_{p,-10}$. The comparison points, $z_{p,+10}$ and $z_{p,-10}$, mark the particle position 10 mm upstream and downstream of the bubble, respectively.

Unfortunately, no difference regarding volume fraction and turbulence intensity was observed. Although, the characterization in Sec. 5.1 emphasized different turbulent intensity between the inflow of the bubbles. Further, the shift from the single-phase liquid flow over the dilute to the dense system should affect the particle movement (Hetsroni, 1989; Sommerfeld, 2017).

One reason for the uniform particle distribution could be the low capability of the tracer particles to follow the fluid flow. Especially, particles interacting with small eddies could detach from the fluid streamlines because of the sudden flow changes. The Stokes number, St, for the PEPT tracer in the water channel was between 0.3 and 193.6 (Eq. 4). The corresponding time scale of the turbulent structures, τ_l, was calculated based on the eddy frequency of the Kolmogorov scale, $\tau_{l,\eta} = \frac{1}{f_\eta} = 0.11\,\mathrm{ms}$, and the frequency of the integral length scale, $\tau_{l,\Lambda} = \frac{1}{f_\Lambda} = 26.7\,\mathrm{ms}$. This leads to the conclusion that the used PEPT tracer followed only the turbulent length scales to a certain extent. Therefore, the tracer particles were affected by turbulent length scales down to $\tau_p \cdot |\overline{\mathbf{u}}| = 1.3\,\mathrm{mm}$. To improve this situation, either particles with a smaller density or diameter are used (Eq. 3), or the liquid velocity increases (Eq. 4).

5.3. Particle displacement around the bubble measured with PEPT

Of particular interest in flotation are the particle trajectories near a bubble and their corresponding interaction. In fact, particle trajectories deviate either in the form of the incident turbulent flow or by the bubble wake. To distinguish the predominant effect in the current setup, the radial particle deviation, $\Delta r(z_p)$, was computed from the PEPT experiment, as seen in Fig. 7. Firstly, each position of the particle trajectory was transformed into cylindrical coordinates, $\mathbf{X_{p,c}} = (r_p, \theta_p, z_p)^T$, based on the center point of the individual bubble, $\mathbf{X_b} = (x_{1,b}, x_{2,b}, x_{3,b})^T$, as origin. Secondly, three positions of each trajectory were chosen, namely, the reference point at the bubble center point, $z_{p,0} = 0\,\mathrm{mm}$, the comparison points 10 mm upstream, $z_{p,+10} = 10\,\mathrm{mm}$, and downstream of the bubble, $z_{p,-10} = -10\,\mathrm{mm}$. Finally, the radial particle deviation, $\Delta r(z_p)$, was calculated as the difference between the radial component of the reference point, $r(z_{p,0})$, and one of the comparison points, $r(z_p) = r(z_{p,+10})$ or $r(z_{p,-10})$,

$$\Delta r(z_p) = r(z_{p,0}) - r(z_p). \tag{15}$$

In Fig. 8, $\Delta r(z_p)$ is plotted over the corresponding radial position at the reference point of each particle trajectory, $r(z_{p,0})$. In this way, the effect of the deviation on the particle trajectory is distinguished between upstream and downstream of the bubble. Further, the predominating tendency is emphasized by arrows in the plots. Only particle trajectories which passed by the bubble with a distance, $|r(z_p)| \leq 10\,\mathrm{mm}$, were used. Each column in Fig. 8 represents one bubble position, $p = 1 - 3$, and each row one volume fraction, $\phi = 0.01\,\%$ and $0.22\,\%$.

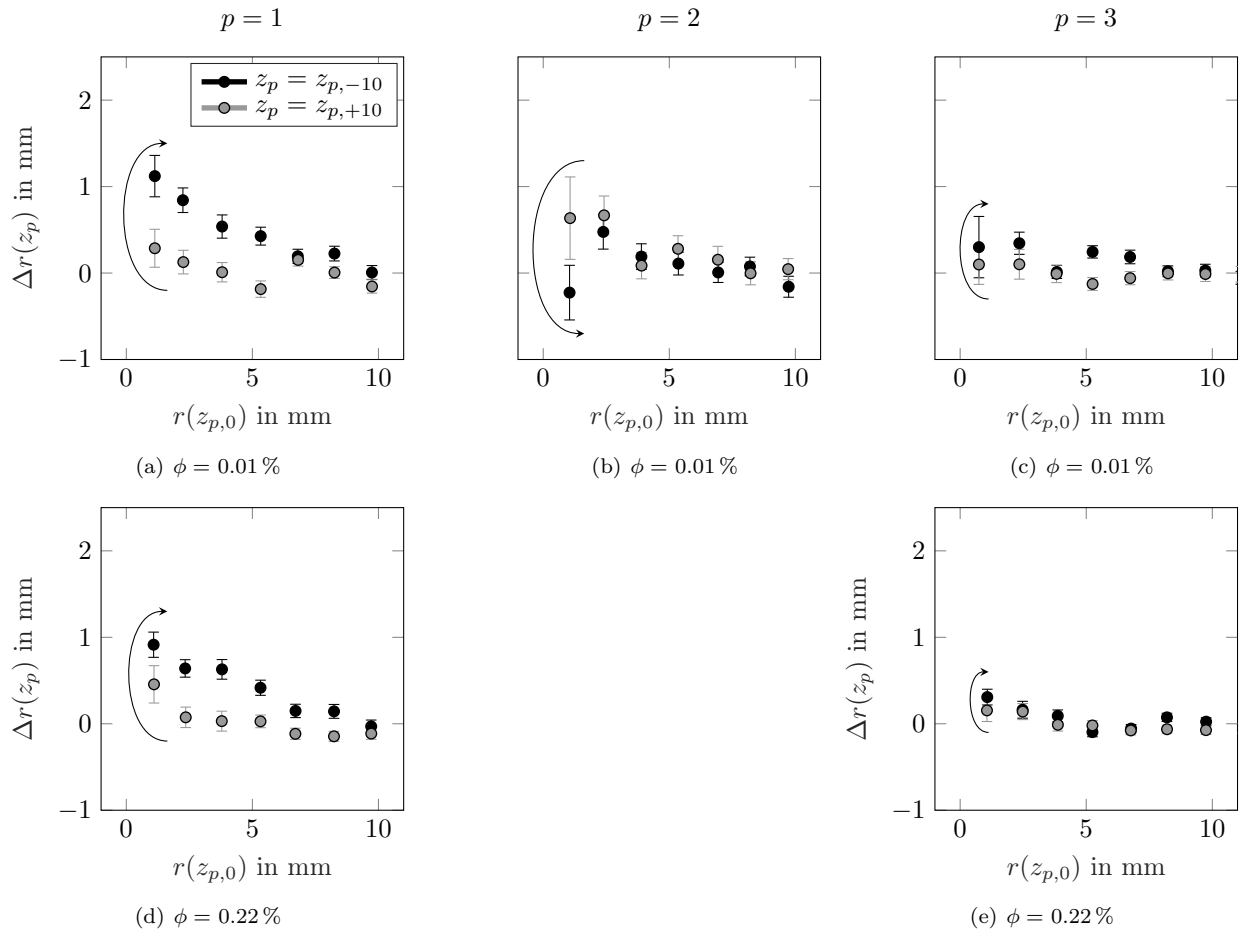

(a) $\phi = 0.01\,\%$ (b) $\phi = 0.01\,\%$ (c) $\phi = 0.01\,\%$

(d) $\phi = 0.22\,\%$ (e) $\phi = 0.22\,\%$

Figure 8: Radial displacement, $\Delta r(z_p)$, of tracer particles measured with PEPT, as illustrated in Fig. 7. The deviation on the particle trajectory is distinguished between upstream, $z_{p,+10}$, and downstream of the bubble, $z_{p,-10}$. The arrow emphasizes the predominating tendency. The trajectory of the tracer particles are binned over the particle radial position at the height of $z_p = 0\,\mathrm{mm} = z_{p,0}$.

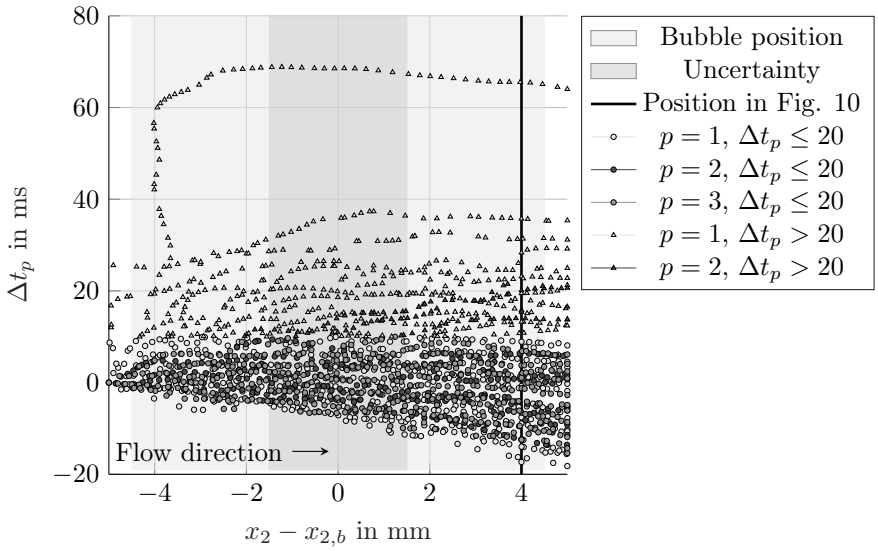

Figure 9: Normalized residence time of particle trajectories, Δt_p, in the near-field of the bubble in x_2-direction measured with PEPT. Each point corresponds to a triangulated particle position belonging to a valid particle trajectory in the near field of each bubble, $x_2 = [-5, 5]\text{mm} + x_{2,b}$. The trajectories are classified by their bubble position, $x_{2,b}$ ($p = 1 - 3$, see Fig. 1), and whether they are above or below the limit of $\Delta t_p = 20\,\text{ms}$.

The data show no significant difference between volume fractions, as seen in Fig. 8(a) and Fig. 8(d) or Fig. 8(c) and Fig. 8(e). Instead, the particle deviation decreases with the turbulence degree from $p = 1$ to $p = 3$ and the distance to the bubble. But, this effect is predominated downstream of the bubble at $z_{p,-10}$, and thus, the particle trajectories were not deviated by the turbulent inflow. One reason could be an interaction of the stagnant bubble with the turbulent inflow leading to a higher oscillation frequency and a change of the wake structures of the bubble. The wake of the bubble at position, $p = 1$, may consisted turbulent length scales larger than 1.3 mm, in contrast to position, $p = 2$ or $p = 3$. Therefore, the particles were pushed further away by these length scales.

5.4. Bubble-particle encounters measured with PEPT

Another option to analyse the bubble-particle interaction is the individual observation of particle trajectories in the near field of the bubble with PEPT for possible encounters. Unfortunately, no particle attachment occurred on a bubble during the measurement of 4599 trajectories over 47.9 h within the ROI. Consequently, no validation case of a bubble-particle encounter existed which is a requirement of an attachment. Therefore, possible particle encounters were classified based on their deceleration in the collision process.

To separate a bubble-particle encounter from a non-encounter, Fig. 9 and Fig. 10 summarize the residence time of all particle trajectories in the near field of each bubble, $x_2 = [-5, 5]\text{mm} + x_{2,b}$. Each point corresponds to a triangulated particle position belonging to a valid particle trajectory. The residence time, $\Delta t_p(x_{2,p})$, refers to the time a particle takes from the reference height, $x_2 = -5\,\text{mm} + x_{2,b}$, to each triangulated position along the main flow direction till $x_2 = 5\,\text{mm} + x_{2,b}$. Further, $\Delta t_p(x_{2,p})$ was normalized by the mean residence time, $\overline{\Delta t_l}$. The mean residence time corresponds to the time a particle, moving with the average liquid velocity, $|\mathbf{u}|$, takes from the reference height to each triangulated position along the main flow direction, $x_{2,p}$,

$$\overline{\Delta t_l}(x_{2,p}) = \frac{10\,\text{mm} - (x_{2,b} - x_{2,p})}{|\mathbf{u}|}. \tag{16}$$

Consequently, the normalization emphasizes the extension of the residence time of the particle. This yields

to

$$\Delta t_p(x_{2,p}) = (t(x_{2,p}) - t_0) - \overline{\Delta t_l}(x_{2,p}), \tag{17}$$

where t is the time step belonging to the tracer position, $\mathbf{X_p}$, and t_0 is the time step of the tracer at the reference height. Additionally, to avoid uncertainties regarding the channel borders, the evaluated cross-section included only the area of $x_1 = [-5, 5]$ mm and $x_3 = [5, 25]$ mm.

Fig. 9 illustrates that only a minority of particle trajectories extended their residence time above the limit of 20 ms in the near field of the bubble. These particle trajectories were located mainly around the upper bubble position with the highest turbulent degree. The majority of particles remained their velocity and even accelerated slightly downstream of the bubble. Only one trajectory had a remarkable higher normalized residence time in the order of 70 ms.

However, Fig. 9 shows only that particles prolonged their residence time, but, refuses to give information regarding the distance between bubble and particle. Therefore, Fig. 10 shows the dependency between the radial position, r, and the normalized residence time. The radial position equals the transformation of the particle position into cylindrical coordinates, $\mathbf{X_{p,c}} = (r_p, \theta_p, z_p)^T$, with the bubble position, $\mathbf{X_b}$, as origin (Fig. 7). In Fig. 10, the radial position, r, of all particle trajectories at $z_p = -4$ mm are summarized. The diagram emphasizes that an increase in residence time is not only caused by the bubble. Also, particle trajectories further away from the bubble exceed a residence time of 20 ms. Besides a bubble-particle interaction, another reason could be the turbulent length scales upstream of the upper bubble. The tracer particle was trapped within the larger eddies leading to higher residence time. The only promising trajectory in Fig. 9 was located in the near-field of the bubble. But based on one individual event, no conclusion regarding a bubble-particle collision can be drawn.

Tu sum up, a bubble-particle encounter was not definitely observed. Reasons for this were, on the one hand, the low number of collisions as only the interaction of individual radiolabeled particles with single bubbles are observable with PEPT. A possible solution would be the employment of a large number of tracers. Based on the triangulation of LORs within a small ROI, six tracers led only to discard of less than 5 % of the data. Further enhancement could be achieved by a reduction of the cross-section of the water channel or minimizing the residence time of a tracer by increasing the flow rate.

On the other hand, the dependency of the temporal and spatial resolution of the tracer position on its activity limited the quality of the triangulated trajectory. The exponential decay of the tracer radionuclide led to a decrease in the spatial resolution for a fixed temporal resolution over time. Consequently, even if an interaction took place, the event of approx. 14 ms could not be resolved and detected. Possible approaches that would enhance the temporal resolution include an increase of the initial tracer activity, the usage of different isotopes with longer half lives, and tailored PEPT cameras optimized for this particular study.

6. Conclusion

This study used PEPT as a method to research the particle distribution and bubble-particle interactions in a turbulent and dense flow field. A water channel equipped with an upstream grid was developed to produce well-defined turbulence. The generated range of turbulent length scales in the liquid flow (20 µm-4800 µm) was characterized by tomographic PIV. The turbulent intensity changed with the distance to the grid (5 % to 15 %), leading to different inflow conditions for each bubble position. Based on the power spectra, nearly isotropic turbulence had been achieved for the middle and lower bubble position (Fig. 5). One shortcoming of the study was the limited number of collision and attachment events of PEPT tracers. Regardless, the influence of turbulence on the particles were observed based on the deviation of the particle trajectory (Fig. 8(a) and 8(d)) and longer residence time (Fig. 9 and Fig. 10). The PEPT enabled the measurements within an opaque flow consisting of a high particle concentration ($\phi = 0.22$ %), which could not be achieved with optical particle tracking methods. As a consequence, these experiments have extended the range of fundamental studies on bubble-particle interactions and provide a foundation to enhance the understanding of turbulence within a flotation cell.

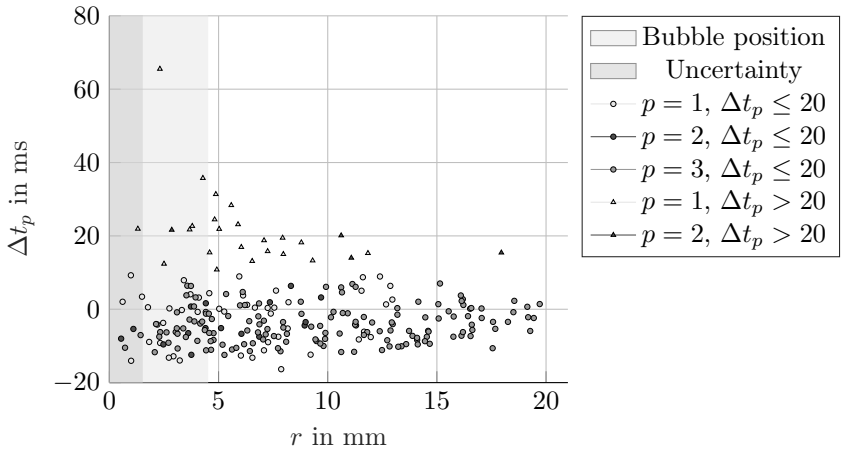

Figure 10: Normalized residence time of particle trajectories, Δt_p, in the near-field of the bubble, depending on its radial position, r, measured with PEPT. The radial position equals the transformation of the particle position into cylindrical coordinates, $\mathbf{X_{p,c}} = (r_p, \theta_p, z_p)^T$, with the bubble position, $\mathbf{X_b}$, as origin (Fig. 7). Each point corresponds to a triangulated particle position of a valid particle trajectory at $z_p = -4\,\text{mm}$. The trajectories are classified by their bubble position, $x_{2,b}$ ($p = 1 - 3$, see Fig. 1) and whether they are above or below the limit of $\Delta t_p = 20\,\text{ms}$.

7. Acknowledgements

This project has received funding from the European Union's Horizon 2020 research and innovation program FineFuture under grant agreement No 821265.

We thank Ms Katharina Haase (Universität der Bundeswehr München, Institute of Fluid Mechanics and Aerodynamics, Germany) for assistance with the design of the water channel, and Dr Angus Morrison (Julius Kruttschnitt Mineral Research Centre, Sustainable Minerals Institute, Australia) for comments that greatly improved the adaption of the water channel to the PET scanner. We also express gratitude to Ms Martina Roßner from the metallurgical laboratory for the preparation of the tracer micrographs.

References

Atkinson, C., Coudert, S., Foucaut, J.M., Stanislas, M., Soria, J., 2010. The accuracy of tomographic particle image velocimetry for measurements of a turbulent boundary layer. Experiments in Fluids 50, 1031–1056. doi:10.1007/s00348-010-1004-z.

Basařová, P., Machoň, V., Hubička, M., Horn, D., 2010. Collision processes involving a single rising bubble and a larger stationary spherical particle. International Journal of Mineral Processing 94, 58–66. doi:10.1016/j.minpro.2009.11.004.

Boucher, D., Jordens, A., Sovechles, J., Langlois, R., Leadbeater, T.W., Rowson, N.A., Cilliers, J.J., Waters, K.E., 2017. Direct mineral tracer activation in positron emission particle tracking of a flotation cell. Minerals Engineering 100, 155–165. doi:10.1016/j.mineng.2016.10.022.

Brady, M.R., Telionis, D.P., Vlachos, P.P., Yoon, R.H., 2006. Evaluation of multiphase flotation models in grid turbulence via particle image velocimetry. International Journal of Mineral Processing 80, 133–143. doi:10.1016/j.minpro.2006.03.010.

Buffler, A., Govender, I., Cilliers, J.J., Parker, D.J., Franzidis, J.P., Mainza, A., Newman, R.T., Powell, M., Westhuizen, A.V.D., 2010. Pept cape town: a new positron emission particle tracking facility at ithemba labs, in: Proceedings Of International Topical Meeting On Nuclear Research Applications And Utilization Of Accelerators, 4-8 May 2009, Vienna: IAEA Proceedings Cd Series Iaea-I3-Cn-173.

Clift, R., Grace, J.R., Weber, M.E., 2005. Bubbles, Drops, and Particles (Dover Civil and Mechanical Engineering). Dover Publications.

Cole, K., Buffler, A., Cilliers, J.J., Govender, I., Heng, J.Y.Y., Liu, C., Parker, D.J., Shah, U.V., van Heerden, M.R., Fan, X., 2014. A surface coating method to modify tracers for positron emission particle tracking (PEPT) measurements of froth flotation. Powder Technology 263, 26–30. doi:10.1016/j.powtec.2014.04.083.

Cole, K., Buffler, A., van der Meulen, N.P., Cilliers, J.J., Franzidis, J.P., Govender, I., Liu, C., van Heerden, M.R., 2012. Positron emission particle tracking measurements with 50 micron tracers. Chemical Engineering Science 75, 235–242. doi:10.1016/j.ces.2012.02.053.

Cole, K., Waters, K., Parker, D., Neethling, S., Cilliers, J., 2010a. PEPT combined with high speed digital imaging for particle tracking in dynamic foams. Chemical Engineering Science 65, 1887–1890. doi:10.1016/j.ces.2009.10.010.

Cole, K., Waters, K.E., Fan, X., Neethling, S.J., Cilliers, J.J., 2010b. Combining positron emission particle tracking and image analysis to interpret particle motion in froths. Minerals Engineering 23, 1036–1044. doi:10.1016/j.mineng.2010.05.012.

Comte-Bellot, G., Corrsin, S., 1971. Simple eulerian time correlation of full-and narrow-band velocity signals in grid-generated, 'isotropic' turbulence. Journal of Fluid Mechanics 48, 273–337. doi:10.1017/s0022112071001599.

Davies, E.R., 2004. Machine Vision: Theory, Algorithms, Practicalities (Signal Processing and its Applications). Morgan Kaufmann.

Evans, G.M., Doroodchi, E., Lane, G.L., Koh, P.T.L., Schwarz, M.P., 2008. Mixing and gas dispersion in mineral flotation cells. Chemical Engineering Research and Design 86, 1350–1362. doi:10.1016/j.cherd.2008.07.006.

Fallenius, K., 1987. Turbulence in flotation cells. International Journal of Mineral Processing 21, 1–23. doi:10.1016/0301-7516(87)90002-0.

Foucaut, J.M., Carlier, J., Stanislas, M., 2004. PIV optimization for the study of turbulent flow using spectral analysis. Measurement Science and Technology 15, 1046–1058. doi:10.1088/0957-0233/15/6/003.

Haase, K., Kück, U.D., Thöming, J., Kähler, C.J., 2017. Emulation of bubble-induced turbulence using randomly moving particles in a grid structure. Chemical Engineering & Technology 40, 1502–1511. doi:10.1002/ceat.201600687.

Hassanzadeh, A., Firouzi, M., Albijanic, B., Celik, M.S., 2018. A review on determination of particle–bubble encounter using analytical, experimental and numerical methods. Minerals Engineering 122, 296–311. doi:10.1016/j.mineng.2018.04.014.

Hetsroni, G., 1989. Particles-turbulence interaction. International Journal of Multiphase Flow 15, 735–746. doi:10.1016/0301-9322(89)90037-2.

Kurian, T., Fransson, J.H.M., 2009. Grid-generated turbulence revisited. Fluid Dynamics Research 41, 021403. doi:10.1088/0169-5983/41/2/021403.

Leadbeater, T.W., Parker, D.J., Gargiuli, J., 2012. Positron imaging systems for studying particulate, granular and multiphase flows. Particuology 10, 146–153. doi:10.1016/j.partic.2011.09.006.

Meng, J., Tabosa, E., Xie, W., Runge, K., Bradshaw, D., Manlapig, E., 2016. A review of turbulence measurement techniques for flotation. Minerals Engineering 95, 79–95. doi:10.1016/j.mineng.2016.06.007.

Nguyen, A., Schulze, H.J., 2003. Colloidal Science of Flotation (Surfactant Science). CRC Press.

Nguyen, A.V., An-Vo, D.A., Tran-Cong, T., Evans, G.M., 2016. A review of stochastic description of the turbulence effect on bubble-particle interactions in flotation. International Journal of Mineral Processing 156, 75–86. doi:10.1016/j.minpro.2016.05.002.

Nguyen, A.V., Kmeť, S., 1992. Collision efficiency for fine mineral particles with single bubble in a countercurrent flow regime. International Journal of Mineral Processing 35, 205–223. doi:10.1016/0301-7516(92)90034-t.

Parker, D.J., Broadbent, C.J., Fowles, P., Hawkesworth, M.R., McNeil, P., 1993. Positron emission particle tracking - a technique for studying flow within engineering equipment. Nuclear Instruments and Methods in Physics Research Section A: Accelerators, Spectrometers, Detectors and Associated Equipment 326, 592–607. doi:10.1016/0168-9002(93)90864-e.

Pope, S.B., 2000. Turbulent Flows. Cambridge University Pr.

Roach, P.E., 1987. The generation of nearly isotropic turbulence by means of grids. International Journal of Heat and Fluid Flow 8, 82–92. doi:10.1016/0142-727x(87)90001-4.

Scarano, F., 2012. Tomographic PIV: principles and practice. Measurement Science and Technology 24, 012001. doi:10.1088/0957-0233/24/1/012001.

Schubert, H., 1999. On the turbulence-controlled microprocesses in flotation machines. International Journal of Mineral Processing 56, 257–276. doi:10.1016/s0301-7516(98)00048-9.

Sciacchitano, A., Wieneke, B., 2016. PIV uncertainty propagation. Measurement Science and Technology 27, 084006. doi:10.1088/0957-0233/27/8/084006.

Sommer, A.E., Nikpay, M., Heitkam, S., Rudolph, M., Eckert, K., 2018. A novel method for measuring flotation recovery by means of 4d particle tracking velocimetry. Minerals Engineering 124, 116–122. doi:10.1016/j.mineng.2018.05.006.

Sommerfeld, M., 2017. Numerical methods for dispersed multiphase flows, in: Particles in Flows. Springer International Publishing, pp. 327–396. doi:10.1007/978-3-319-60282-0_6.

Sovechles, J.M., Boucher, D., Pax, R., Leadbeater, T.W., Sasmito, A.P., Waters, K.E., 2017. Performance analysis of a new positron camera geometry for high speed, fine particle tracking. Measurement Science and Technology 28, 095402. doi:10.1088/1361-6501/aa7dce.

Tokuhiro, A., Maekawa, M., Iizuka, K., Hishida, K., Maeda, M., 1998. Turbulent flow past a bubble and an ellipsoid using shadow-image and PIV techniques. International Journal of Multiphase Flow 24, 1383–1406. doi:10.1016/s0301-9322(98)00024-x.

Waters, K.E., Rowson, N.A., Fan, X., Cilliers, J.J., 2009. Following the path of hydrophobic and hydrophilic particles in a denver cell using positron emission particle tracking. Asia-Pacific Journal of Chemical Engineering 4, 218–225. doi:10.1002/apj.224.

Waters, K.E., Rowson, N.A., Fan, X., Parker, D.J., Cilliers, J.J., 2008. Positron emission particle tracking as a method to map the movement of particles in the pulp and froth phases. Minerals Engineering 21, 877–882. doi:10.1016/j.mineng.2008.02.007.

Yuen, H.K., Princen, J., Illingworth, J., Kittler, J., 1990. Comparative study of hough transform methods for circle finding. Image Vision Comput. 8, 71–77.